Fast Aquatic Escape with a Jet Thruster

R. Siddall* and M. Kovac*

***Abstract*—The ability to collect water samples rapidly with aerial-aquatic robots would increase the safety and efficiency of water health monitoring, and allow water sample collection from dangerous or inaccessible areas. An Aquatic Micro Air Vehicle (AquaMAV) able to dive into the water offers a low-cost and robust means of collecting samples. However, small scale flying vehicles generally do not have sufficient power for transition to flight from water. In this paper we present a novel jet propelled AquaMAV able to perform jumpgliding leaps from water, and a planar trajectory model that is able to accurately predict aquatic escape trajectories. Using this model, we are able to offer insights into the stability of aquatic take-off to perturbations from surface waves, and demonstrate that an impulsive leap is a robust method of flight transition. The AquaMAV uses a CO_2 powered water jet to escape the water, actuated by a custom shape memory alloy gas release. The 100 gram robot leaps from beneath the surface, where it can deploy wings and glide over the water, achieving speeds above 11 m/s.**

I. Introduction

Locomotion in unstructured terrain is a significant challenge to robots operating in an outdoor environment, often requiring multiple modes of operation. For an aerial robot, movement in water creates additional structural and propulsive design constraints that can be difficult to overcome [1]. However, the ability to move in air and water would allow unique robot operation in a wide variety of oceanic, riverine or urban environments. We are developing an AquaMAV capable of diving directly into the water and retaking flight using a high powered burst of thrust (Fig. 1).

An aerial-aquatic robot would find use in disaster relief or water ecology, particularly where access is limited such as flooded towns or littoral areas. In these unstructured aquatic environments, obstacles impede conventional aquatic vehicles, and prevent close observation by aerial robots. Flight allows targets to be reached rapidly from outside hazardous zones, at speeds that cannot be matched by man-portable aquatic robots. During an emergency scenario such as a stricken ship or a tsunami event, an AquaMAV could dive into an isolated area of water, where it could collect water samples and record environmental data. The vehicle could then perform a short take-off (Fig. 1), and return to its launch site to submit collected samples and data. This would enable a fast, targeted response to emergencies that could not be matched by current systems.

The efficacy of water sampling with aerial robots using larger multirotor platforms has been demonstrated [2]. This approach relies on accurate sensing and control to maintain position while a sample probe is lowered. However, a fixed wing vehicle provides greater range and speed than hovering vehicles, and plunge diving reduces the need for accurate control, allowing platforms to be produced at lower cost and operated in larger numbers.

The speed and range of robotic aircraft may not always be required by a mission, but aerial-aquatic locomotion has broader advantages in robot mobility. Many amphibious terrestrial robots have been implemented [3], [4], but these robots are not able to cross large, sheer obstacles, and often can only exit the water on gentle inclines. Buoyant 'floatplane' UAVs [1] will be similarly inhibited by obstacles or waves on the water, which will prevent taxiing take-off in constrained spaces.

Several large (2-3m wingspan) unmanned seaplanes are currently in operation [1], [5], and experimental studies have shown the potential of an aerial-aquatic robot propelled by adaptable flapping wings [6]. Other work has demonstrated the efficacy of jumpgliding locomotion in terrestrial robots [7], [8], and fixed wing Micro Air Vehicles (MAVs) have been implemented with terrestrial mobility [9]. Aquatic locomotion by quadrotors has been shown [10], but to the best of the author's knowledge, no fixed wing AquaMAV has been realised to date.

*Department of Aeronautics, Imperial College London

Manuscript received March 26, 2015; revised July 18, 2016. This work was funded by the UK Engineering and Physical Sciences Research Council.



Fig. 1: Outdoor testing of the presented prototype: An AquaMAV can return water samples and data from isolated areas of water, using a powerful burst of water jet thrust to accelerate free of the water and transition to flight. A: The AquaMAV launches itself out of water. B: Timelapse of a launch trajectory. Wings are deployed in the final snapshot.

A. *Principles for Aquatic Escape*

Underwater locomotion is one of the most energetically efficient forms of locomotion in the animal kingdom [11], principally because a neutrally buoyant animal is not required to resist its own gravity to swim. However, neutral buoyancy is often opposed to the constraints of flight. This becomes most apparent when attempting to leave the water surface, where propulsive and lifting surfaces must be kept out of water to develop forces, made more difficult by motion of the water surface. Without additional buoyancy control, water escape will be extremely difficult for aerial-aquatic vehicles.

A buoyant quadcopter can allow itself sufficient buoyancy to clear its propeller from the water for take-off, or partially lift out of the water using additional rotors [10]. Thrust from aerial propellers can be used for swimming, but motors would have to operate off-design at low speeds when underwater, greatly reducing efficiency unless variable gearing is used. Another drawback is that such a vehicle would require a calm surface to take-off, while the principle advantage would be that it allows multiple swimming and flying phases in a single mission. However, we propose that for high frequency single sample return missions, the most robust system would be a short burst of thrust, launching a fixed wing vehicle through the surface to return to base.

In nature, several species of squid are able to initiate gliding leaps by expelling a pressurised jet of water [12]. This jet propelled launch is uniquely applicable to short take-offs by AquaMAVs. Jets of mass have a very rapid thrust response, unlike swimming leaps, and a jet continues to produce thrust in both air and water because it does not rely on external reaction forces. This allows a vehicle to escape the water and accelerate when airborne, where drag is dramatically reduced compared to in water [11]. While this could also be achieved with combustible rockets, rocket propellants are often hazardous, and many operating environments (such as an oil spill) may preclude the use of combustion. A water jet offers a clean and safe alternative.

When leaving the water, both flying squid [12] and flying fish [11] keep their wings folded until they are clear of the surface. There are large differences in fluid forces between the two media, and doing this protects wing structures from large hydrodynamic loads, reduces drag, and may also have stability considerations (Section III-B). Reconfigurable wings have also been shown to have advantages in jumpgliding [8], and are features of almost all aerial aquatic animals [1].

In this paper we will present an AquaMAV capable of gliding leaps from beneath the water. The robot launches using a powerful water jet, powered by controlled release of a 5ml tank of 57 bar CO_2 gas. The robot uses a shape memory alloy actuated valve to control the CO_2 release, and has deployable wings which allow it to maintain stability and minimise drag when leaving the water. These wings are then deployed in the air for gliding. In the following sections, we introduce the physical principles behind water jet propulsion, and detail the key design features of the jet-propelled jumping robot. We use a planar trajectory model to examine the aquatic take-off process, and show that

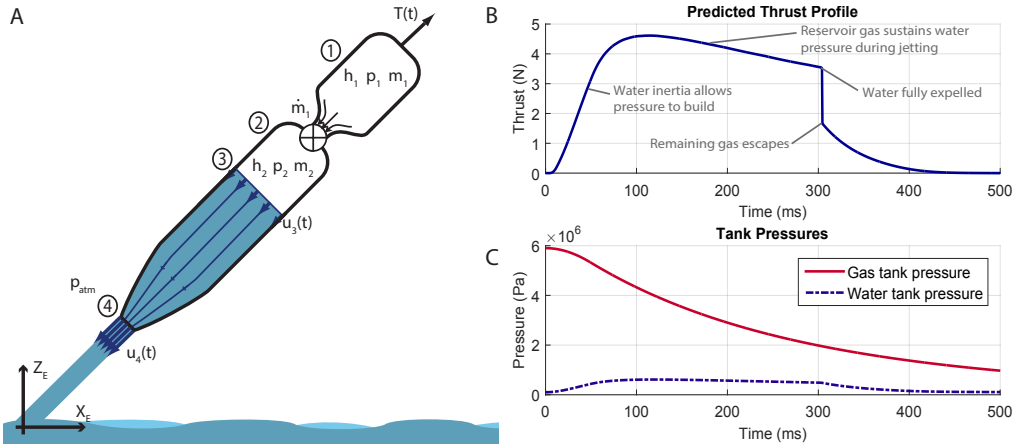


Fig. 2: (A) Jet propulsion principle: Gas released from a high pressure tank expels water, propelling the vehicle. Circled numbers correspond to the locations indicated by equation subscripts. (B) Simulated thrust for water rocket with separated chambers. (C) Gas pressures in water and gas tanks during jetting.

an impulsive jet is a robust means of flight transition. Consistent static thrust from the fabricated device and flight from beneath the water is then demonstrated.

II. Water Jet Propulsion

In this section we use the subscripts 1, 2, 3 and 4 to denote variables relating to the main gas tank, the gas within the water tank, the air-water interface, and nozzle outlet respectively (Fig. 2A). The thrust produced by a jet of mass flow $\dot{m}_4$ and velocity u_4 is given by equation 1. If a gas is used as propellant, its low density means that thrust production is negligible without very high exit velocities, and for efficient propulsion from a limited reservoir, a heavier propellant is preferable. For an AquaMAV, water can easily be collected before launch, with compressed gas powering expulsion.

$$T = \dot{m}_4 u_4 \tag{1}$$

Water's incompressibility means the expelled jet will be at ambient pressure, and the gas expansion rate will equal the water outflow. The water flow within the tank is treated as quasi-1D by assuming uniform axial flow [13]. By mass continuity, the local velocity is then a function of cross-section area (equation 2). The unsteady Bernoulli equation (equation 3) is used, integrating from the air-water interface to the nozzle exit (Fig. 2). Total pressure along a streamline running from 3 to 4 is equal to the instantaneous gas pressure in the water tank.

$$A_3(t)u_3(t) = A_4 u_4(t) \tag{2}$$

$$\int_3^4 \frac{\partial u}{\partial t} ds + \frac{p_2}{\rho_w} + \frac{1}{2}(u_4^2 - u_3^2) = 0 \tag{3}$$

Where u is the water velocity, p_2 the gas pressure in the water tank, V_2 the gas volume, A_n the jet cross sectional area and ρ_w the density of water. The pressure acting on the water must be built up by the gas released from the CO_2 tank. To compute the flow rate out of the tank, we follow the valve flow equations given in the European standard EN-60534 ([14], equations 4-7) With the gas tank initially charged to 57 bar, the outflow will be choked, and will remain so until the pressure ratio (equation 5) falls below κ_{choke} (equation 6). Υ is a compressibility correction factor (equation 7).

$$\dot{m}_1 = K_v \Upsilon \sqrt{\kappa p_1 \rho_1} \tag{4}$$

$$\kappa' = (p_1 - p_2)/p_1 \tag{5}$$

$$\kappa = \begin{cases} \kappa' & \text{if } \kappa' < \kappa_{choke} \\ \kappa_{choke} & \text{if } \kappa' \geq \kappa_{choke} \end{cases} \tag{6}$$

$$\Upsilon = 1 - \kappa / 3\kappa_{choke} \tag{7}$$

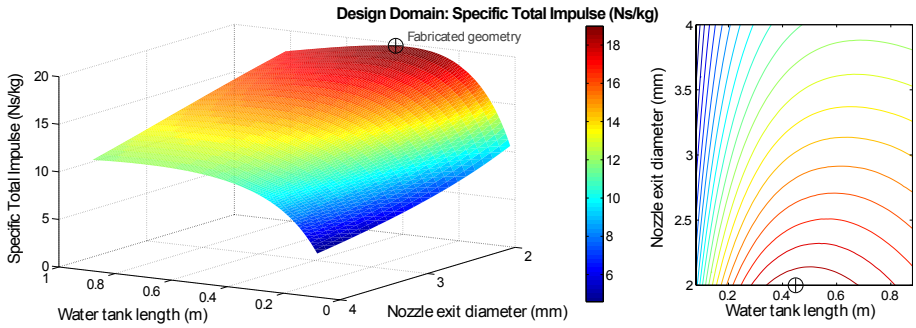


Fig. 3: Design domain: Variation of specific total impulse, showing the existence of an optimal water tank volume for a given gas tank. Decreasing nozzle diameter increases total efficiency, but reduces thrust production, and a minimum of diameter 2mm was set. The prototyped geometry is marked with a ⊕.

Gas flow depends on the valve flow coefficient, K_v, and the limiting pressure ratio, κ_{choke}, the point at which the valve flow becomes sonic. Liquids and gases behave similarly at low pressures [15], so K_v was measured by fixing the valve in the open position and logging the discharged volume against time of a 0.5m tall, 4cm diameter column of water through the valve, and fitting K_v according to the EN-60534 equations for incompressible fluids. κ_{choke} is a compressible property which cannot be measured from water flow, and so was inferred from manufacturer data [16] for air flow at 7 bar based on the measured K_v value, and corrected for the different properties of CO_2 (an ideal CO_2 nozzle chokes at an upstream pressure of 1.8 bar, so we assume sonic conditions for the data at 7 bar).

To determine the variation of gas conditions in the two tanks, a first law energy balance is used. The gas exchange is treated as a quasi-equilibrium, adiabatic process, as jetting takes place over too short a timescale for significant heat transfer to occur. This gives an equation in which the stagnation enthalpy flux from the gas tank ($\dot{m}_1 h_{01}$) is equivalent to the increase in enthalpy and kinetic energy of gas in the water tank ($m_2(h_2+u_3^2/2)$), less the pdV work done against water pressure (equation 8). Gases obey the ideal gas equation of state throughout.

$$\dot{m}_1 h_{01} = \frac{d}{dt}\left[m_2\left(h_2+\frac{u_3^2}{2}\right)\right] - p_2\dot{V}_2 \tag{8}$$

Where h is specific enthalpy (subscript $_0$ denotes a stagnation quantity). Combining equations 1-8 leads to a system of four first and second order differential equations in $V_2(t)$, $\dot{V}_2(t)$, $h_1(t)$, $h_2(t)$ and $m_1(t)$. These equations remain valid until all water is expelled, after which the release of remaining gas produces a small amount of thrust. At this stage, total gas mass inside the thruster (m_1+m_2) is no longer conserved, equation 8 does not hold, and the mass flow out of the nozzle must also be included in the thermodynamic calculation (equation 9). To calculate this gas mass flow, the outlet Mach number, M, is calculated based on the outlet stagnation pressure ratio (equation 10).

$$\dot{m}_1 h_{01} = \frac{d}{dt}\left[m_2\left(h_2+\frac{u_3^2}{2}\right)\right] - \dot{m}_4 h_{02} \tag{9}$$

$$\frac{p_4}{p_{02}} = \left(1+\frac{\gamma-1}{2}M^2\right)^{-\frac{\gamma}{\gamma-1}} \tag{10}$$

Where γ is the gas adiabatic index. The conical water nozzle has no diverging section so $M \leq 1$. When subsonic, the outlet will be at atmospheric pressure, but if the pressure ratio is greater than a critical value (equation 11, different to the valve-specific κ_{choke} value), the flow is choked, $M=1$, and the nozzle outlet pressure will be greater than atmospheric. In both cases, the mass flow out can be computed using a standard Mach number relation (equation 12).

$$\frac{p_{atm}}{p_2} = \left(\frac{2}{\gamma+1}\right)^{\frac{\gamma}{\gamma-1}} \tag{11}$$

$$\frac{\dot{m}_4\sqrt{c_p T_{02}}}{A_4 p_{02}} = \frac{\gamma M}{\sqrt{\gamma-1}}\left(1+\frac{\gamma-1}{2}M^2\right)^{-\frac{1}{2}\frac{\gamma+1}{\gamma-1}} \tag{12}$$

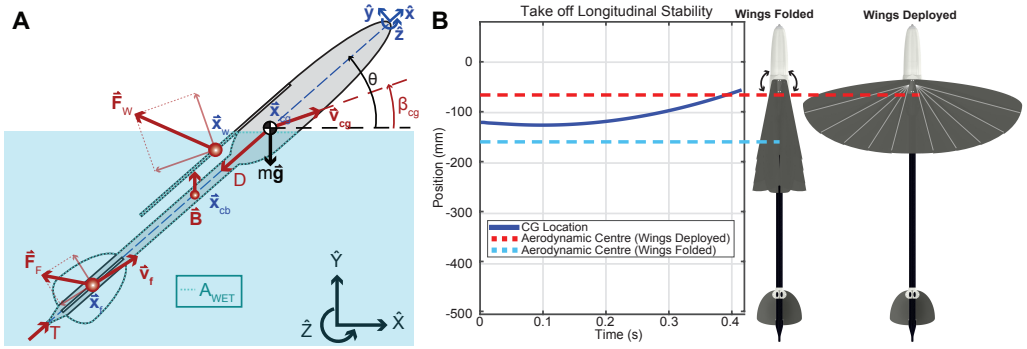


Fig. 4: A: Nomenclature for the equations of motion. B: The AquaMAV centre of gravity as water is expelled during jetting, with the aerodynamic centre of the wings in both configuration shown. Folding the wings moves the aerodynamic centre backward, ensuring stability until all water has been expelled.

Where c_p the gas heat capacity and p_{02} is the stagnation pressure of gas in the water tank). Thrust is given by equation 13 with an additional term to account for the outflow being above atmospheric pressure.

$$T = \dot{m}_4 u_4 - A_4(p_4 - p_{atm}) \tag{13}$$

This system of equations is solved in Matlab with a variable order implicit solver. A conditional statement links the regimes; integration of the water jetting equations is halted once all water is expelled, and final values provide initial conditions to the gas-only equations.

The simulated results for the prototyped thruster are shown in Fig. 2. Initially, the water's inertia limits flow rate, and allows pressure to be built up in the water tank. A small amount of gas thrust can be seen after all water is expelled at 0.3s, reducing rapidly. Due to the high pressures, gas flow through the valve and nozzle are choked throughout jetting.

A. Design Domain

For a given reservoir pressure and valve flow coefficient, the work extracted from the gas can be maximised by varying the water tank size and nozzle diameter. Enlarging the water tank increases launch mass, and an optimum tank volume exists. To obtain this optimum, the specific total impulse (I_{sp}, equation 14) is used as an objective, maximising the momentum imparted to the robot.

$$I_{sp} = \int T dt / m_{total} \tag{14}$$

During jetting, pressure in the water tank is maintained by reservoir gas with a limited flow rate, so a smaller nozzle allows a higher water pressure to be maintained, increasing performance. However, this decreases thrust (equation 1) and a very small nozzle will be insufficient to propel the vehicle. It was decided to target a thrust to weight ratio greater than 5, or 5N of peak thrust, giving a 2mm minimum nozzle exit diameter, rounded for manufacturing. The design domain was computed by numerical integration (Fig. 3), with the specific impulse calculated based on the mass of the thruster alone, excluding the electronics and airframe. This gave an optimum tank length of 0.45m, which was fabricated.

III. Planar Trajectory Model

The robot is fitted with fins and a collapsible wing for flight. To investigate the robustness of the transition to flight from water, we implemented a planar trajectory model and simple estimation of the hydrodynamic forces during water exit (section III-C). Here, we use the subscripts $_w$, $_f$, $_b$, $_{cg}$ and $_{cb}$ to refer to the robot wing, fins, body and centres of gravity and buoyancy respectively. Subscript $_s$ refers to skin friction forces. The trajectory is defined by velocity and acceleration vectors, $\vec{a}$ and $\vec{v}$, in earth fixed inertial axes with unit vectors $\hat{X}$,$\hat{Y}$,$\hat{Z}$. We also define position vectors, $\vec{x}$, within a robot-fixed reference frame rotated by an angle

θ about $\hat{\boldsymbol{Z}}$ from the inertial frame, with its origin at the robot nose and unit vectors $\hat{\boldsymbol{x}}$,$\hat{\boldsymbol{y}}$,$\hat{\boldsymbol{z}}$ (Fig. 4A).

A. Aerodynamics

The vector forces produced by the wing, $\vec{\boldsymbol{F}}_{\boldsymbol{w}}$, and the tail fins, $\vec{\boldsymbol{F}}_{\boldsymbol{f}}$ (equations 15 and 16), have a lift component perpendicular to the local velocity, $\vec{\boldsymbol{v}}$, and a drag component opposing it, defined by lift and drag coefficients C_{lw} and C_{dw} respectively for the main wing, and C_{lf} and C_{df} for the fins.

$$\vec{\boldsymbol{F}}_{\boldsymbol{w}} = \frac{1}{2}\begin{pmatrix} C_{lw} \\ C_{dw} \end{pmatrix}\rho_a A_w |\vec{\boldsymbol{v}}_{cg}|^2 \tag{15}$$

$$\vec{\boldsymbol{F}}_{\boldsymbol{f}} = \frac{1}{2}\begin{pmatrix} C_{lf} \\ C_{df} \end{pmatrix}\rho_a A_f |\vec{\boldsymbol{v}}_f|^2 \tag{16}$$

Where A is the component's lifting area, and ρ_a the density of air. The local velocity of the wing is taken as the velocity of the centre of gravity, $\vec{\boldsymbol{v}}_{\boldsymbol{cg}}$, but the tail velocity, $\vec{\boldsymbol{v}}_{\boldsymbol{f}}$ includes the effect of the vehicle's pitch rate, $\dot{\theta}$:

$$\vec{\boldsymbol{v}}_f = \vec{\boldsymbol{v}}_{cg} + \boldsymbol{R}(\pi/2-\theta)(\dot{\theta}\hat{\boldsymbol{Z}} \times \vec{\boldsymbol{x}}_f) \tag{17}$$

Where $\boldsymbol{R}$ is a matrix representing rotation about $\hat{\boldsymbol{Z}}$. The main wing is initially retracted into a low aspect ratio (AR_w) delta configuration (Fig. 4B) which produces significant vortex lift, and so the Polhamus suction analogy is used to compute C_{lw} and C_{dw} (equations 18 and 19, with constants k_p and k_v taken from [17]). Once open, the wing has a high aspect ratio, and C_{lw} and C_{dw} become the coefficients of an elliptic flat plate (equations 20 and 21). In the model, wing deployment is treated as instantaneous, represented by a step change in lift behaviour at time $t = t_d$.

$$C_{lw} = k_p sin(\alpha_w)cos^2(\alpha_w) + k_v sin^2(\alpha_w)cos(\alpha_w) \tag{18}$$

$$C_{dw} = k_p sin^2(\alpha_w)cos(\alpha_w) + k_v sin^3(\alpha_w) \tag{19}$$

while: $t < t_{deploy}$

$$C_{lw} = 2\pi(\alpha_w)/(1+2\mathit{AR}_w^{-1}) \tag{20}$$

$$C_{dw} = C_{lw}^2/(\pi \mathit{AR}_w) \tag{21}$$

while: $t \geq t_{deploy}$

Parameter	Value		Unit
	Retracted	*Deployed*	
Wing Area, A_w	126	475	cm^2
Wing Aspect Ratio, AR_w	0.79	4.26	-
Wing Span	100	450	mm
Wing Chord	210	132	mm
Polhamus constants (k_P, k_V)	0.7, 3		-
Tail Area, A_f	50		cm^2
Tail Aspect Ratio, AR_f	1.4		-
Body wetted surface area, A_b	278		cm^2
Body Width, BW	36		mm
Body Length, BL	552		mm

TABLE I: Key robot parameters.

The fin coefficients, C_{lf} and C_{df} have the same form as equations 20 and 21. The angles of attack of the main wing and fins, α_w and α_f, are calculated from the angle the component's velocity in the inertial frame makes with the horizontal, denoted by β. β_f includes pitch damping effects (equation 17), while pitching of the main wing is neglected.

$$\alpha_w = \theta - \beta_{cg} + \alpha_0 \tag{22}$$

$$\alpha_f = \theta - \beta_f \tag{23}$$

Where α_0 is the preset wing incidence relative to the robot's longitudinal axis, fixed at 7^o. The deployed wing's planform (table I) means that with no incidence on the tail fins the AquaMAV must travel at 8.5m/s to produce sufficient lift to balance its 100 gram weight.

B. Longitudinal Stability

The location of the jet centre of mass, $\vec{\boldsymbol{x}}_{cg}$, and the moment of inertia about that centre, I_{yy}, changes as water is expelled from the tank. The movement of $\vec{\boldsymbol{x}}_{cg}$ is of particular importance to the transition to flight, as it has significant effect on the longitudinal aerodynamic stability. Retraction of the wing ensures stability during launch by moving the aerodynamic centre of the main wing, $\vec{\boldsymbol{x}}_w$, rearward (Fig. 4B). Once all water is expelled, $\vec{\boldsymbol{x}}_{cg}$ is ahead of the deployed wing quarter chord, and the wings can open to a larger, higher aspect ratio configuration for flight.

C. Water Resistance

The equations for C_l and C_d neglect friction, so we also include an additional drag force, D (equation 24).

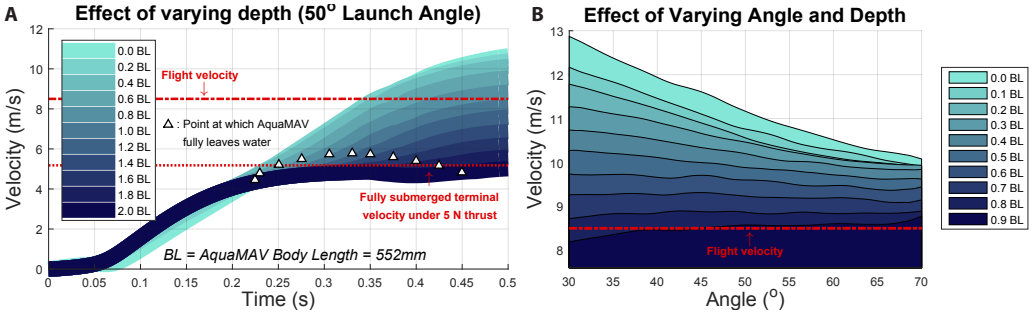


Fig. 5: The effect of perturbations on aquatic take-off. A: The effect of increasing the depth of the robot beneath the water (50^o start angle). Depth is in body lengths (BL) below the free floating position. Escape speed is limited by drag, but the robot achieves flight speed at up to 1BL. B: The effect of both depth and launch angle on the robot velocity after jetting. At up to 0.8BL the robot reaches flight speed in spite of perturbations to launch angle.

The jet body is slender and streamlined (Fig. 4B), and the fins and wings are made from thin flat plates, so drag at zero angle of attack will be dominated by skin friction forces. In order to estimate the viscous force on the wings and fins, we use a turbulent flow flat plate skin friction coefficient, using a Reynolds number (Re) based on retracted wing cord to estimate friction on the lifting surfaces (equation 25). To compute body drag this coefficient is modified based on the ratio of the body's maximum width and length (BW/BL, equation 26) [18]. D acts through the robot's centre of gravity, in the negative $\hat{\boldsymbol{x}}$ direction.

$$D = \frac{\rho_a}{2}(C_s(2A_w + 4A_f) + C_{sb}A_b)|\vec{\boldsymbol{v}}_{\boldsymbol{cg}}.\hat{\boldsymbol{x}}|\vec{\boldsymbol{v}}_{\boldsymbol{cg}}.\hat{\boldsymbol{x}} \quad (24)$$

$$C_s = 0.0307Re^{-1/7} \quad (25)$$

$$C_{sb} = C_s\left(1 + \frac{3}{2}(BW/BL)^{\frac{3}{2}} + 7(BW/BL)^3\right) \quad (26)$$

The robot is actuated while floating on the surface of the water, and has slight positive buoyancy, such that its nose just breaks the surface. As it accelerates out of the water, drag acting on the vehicle will limit its velocity. At each timestep, the model calculates from the robot position and orientation the fraction of each surface that is immersed in the water. Neglecting Reynolds number changes, the only fluid specific variable in equations 15-26 is the fluid density. We can therefore introduce a factor, Q (equation 27):

$$Q = \left(\frac{\rho_w}{\rho_a}\frac{A_{wet}}{A_{total}} + \left(1 - \frac{A_{wet}}{A_{total}}\right)\right) \quad (27)$$

Where A_{wet} and A_{total} are the submerged and total areas of the component in question. This approximation neglects any motion of the water surface, and assumes that the flow around a partially immersed surface is similar to the flow at the same point on a fully immersed surface (a similar assumption is made for water impact analysis in [19]). We also neglect any change in the point of action of forces during aquatic escape. Despite these assumptions, this approach is capable of producing good predictions of speeds as the robot leaves the water (section VI).

The robot floats on the water surface prior to launch, so buoyancy must also be included. The immersed volume of the robot, V_{wet}, is calculated at each timestep, giving a buoyant force, $\vec{\boldsymbol{B}}$, which acts vertically, and its point of action, $\vec{\boldsymbol{x}}_{cb}$ (equation 28, where g is gravitational acceleration).

$$\vec{\boldsymbol{B}} = \rho_w g V_{wet}\hat{\boldsymbol{Y}} \quad (28)$$

The forces acting on the robot are resolved into inertial axes, and moments are taken about $\boldsymbol{x}_{cg}$ (equation 29 and 30). The thrust, T, used for the integration is the mean of 6 experimental thrust profiles (section V), from which the mass of water remaining in the tank is also calculated. The resulting equations of motion are integrated numerically using a Runge-Kutta solver in Matlab.

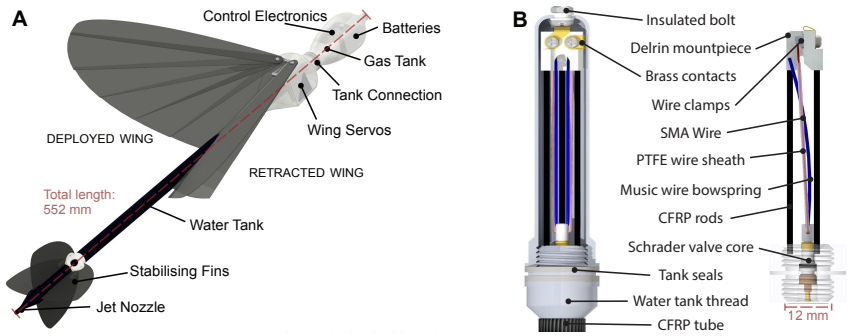


Fig. 6: CAD renderings of the fabricated AquaMAV prototype. A: Component placement within the AquaMAV and the two wing configurations. B: Close up of the gas tank and the self contained, removeable SMA gas release system.

$$m\vec{\boldsymbol{a}} = \vec{\boldsymbol{B}} - m\vec{\boldsymbol{g}} + \boldsymbol{R}(\theta-\alpha_w)Q_w\vec{\boldsymbol{F}}_w + \boldsymbol{R}(\theta)(T-DQ_s)\hat{\boldsymbol{x}} + \boldsymbol{R}(\theta-\alpha_f)Q_f\vec{\boldsymbol{F}}_f \tag{29}$$

$$I_{yy}\ddot{\theta}\hat{\boldsymbol{z}} = (\vec{\boldsymbol{x}}_w - \vec{\boldsymbol{x}}_{cg})\times\boldsymbol{R}(\alpha_w)Q_w\vec{\boldsymbol{F}}_w + (\vec{\boldsymbol{x}}_{cb} - \vec{\boldsymbol{x}}_{cg})\times\boldsymbol{R}(\theta)\vec{\boldsymbol{B}} + (\vec{\boldsymbol{x}}_f - \vec{\boldsymbol{x}}_{cg})\times\boldsymbol{R}(\alpha_f)Q_f\vec{\boldsymbol{F}}_f - \dot{I_{yy}}\dot{\theta}\hat{\boldsymbol{z}} \tag{30}$$

D. Take-off Robustness

The simple drag model was found to give a good prediction of the acceleration profile of the AquaMAV during aquatic take-offs (section VI). The model was therefore used to evaluate the robustness of take-off to external perturbations which can occur in an outdoor environment. Wave motion over the floating vehicle can perturb the vehicle angle when it is actuated, and instantaneously submerge the robot, creating an additional distance to traverse underwater.

Increasing depth has a strong effect on the final velocity, as drag greatly limits underwater speed (Fig. 5A). Equating drag (equation 24) when fully submerged with wings folded to the 5N peak thrust gives a terminal velocity of 5.2 m/s (neglecting lift and buoyancy), which the robot velocity after jetting tends toward as depth increases. Simulating launches at several different angles and depths, the simulation indicates that the jet will be able to achieve its minimum flight velocity (8.5m/s) regardless of angle as long as it is not submerged more than $0.8BL$ beneath the surface (Fig. 5B). Launching the robot nearer to vertical results in lower speed (but higher altitude). More interestingly, a steeper launch makes the robot less sensitive to depth change, because it has a shorter distance to traverse to escape the water.

IV. Prototype

The fabricated thruster has an air and water tank, with sealed screw connections to a centrepiece containing a poppet valve (Fig. 6). To contain and release the high pressure gas, an NiTi Shape Memory Alloy (SMA) actuator has been developed. This valve actuator is inside the CO_2 tank, so charging cannisters can be easily attached.

The gas pressure vessel is constructed from 7075 aluminium according to European standards [20], with an extra safety factor of 2 applied to the wall thickness to increase safety. The water tank is pressurised to less than 10bar (Fig. 2C) and sustains pressure only briefly, so is instead made from a woven CRFP tube, bonded to an aluminium screw connection (Fig. 6B) and plastic nozzle. The system has a deliberate modular construction, with the centrepiece and valve actuation system entirely self-contained, so that both tanks can be changed according to final mission requirements.

A. Valve Actuation

The valve is opened by raising the valve stem 1.6mm. Under 57 bar of pressure, the force to open the valve is 24N, (19N of pressure force, 5N from the valve internal spring). These high force, short stroke actuation requirements are well suited to the use of NiTi SMA wire, and an actuation system was designed using 0.51mm wire, which produces repeatable contraction forces of up to

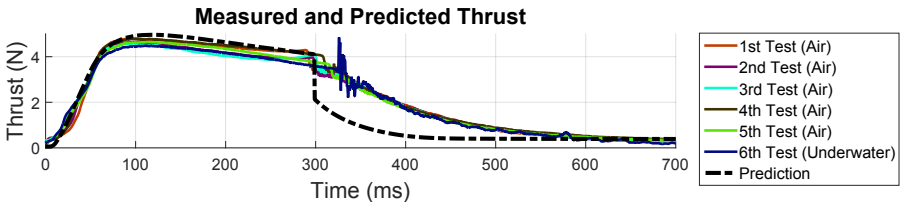


Fig. 7: Thrust test data. Slight inconsistencies in thrust are due to variations of the vapour pressure of the liquid CO_2 in the charging capsule. Test 6 was conducted with the thruster immersed in water.

35.6N upon heating to 90^{o}C [21]. To provide sufficient stroke and force, a single length of 104mm flexinol wire is threaded through the valve stem, creating two 50mm wires (Fig. 6). The wires pull against a frame formed by carbon fibre rods mounted into the centrepiece.

After contraction, the wires must be stretched to reseal the tank. This requires a minimum stress of 69MPa, corresponding to a force of 27.2N. To achieve this force with minimal mass and volume, two buckling spring steel rods with pinned ends were used. The large deflection buckling behaviour can be solved analytically using elliptical integrals [22]. To achieve the required average force over the valve stroke, with the rod length constrained to be <47mm to fit within the tank, the diameter was set to 0.8mm. This produced a force of 40N, which is near-constant over the stroke range.

To provide an electrical conduit into the pressurised container, the vessel wall is used as a negative earth and an insulated bolt was fastened through the tank end (Fig. 6). Brass contacts are attached to each end of the SMA wire, contacting the vessel wall and bolt when the valve is inserted, forming a complete circuit without compromising the seal. Actuation is controlled by a 100Hz, 9.1A current pulse train (50% duty), lasting for 1s. This is passed through the wire from a 7.4V, 200mAh battery, sufficient for over 150 actuations, and controlled using an Arduino microcontroller. Excluding electronics, the mass of the thruster is 41.9 grams.

In order to leap clear of the water, the jet tank must ingest water from its surroundings. While the water tank will fill gradually with the tail pointing upward in the water, it will not fill when nose up. For testing the tank is currently filled manually, but a future prototype will include a check valve at the opposite end to the nozzle, allowing the tank to fill when unpressurised, but containing the pressure during jetting.

B. *Flight Components*

The AquaMAV is fitted with deployable wings for flight. To reduce complexity these wings are uncambered, fabricated from 0.25mm carbon fibre plates. Each wing is divided into six segments which pivot about a hinge at the leading edge, allowing the wings to sweep backward. Of the six segments, only the leading edge is actuated, while the root segment is fixed to the fuselage. The other four segments are free to rotate, but are linked to the driven leading edge by kevlar twine, such that when the leading edge is rotated the other segments follow.

The wing hinges are actuated by 4.5 gram servos. Two servos are used for symmetry and simplicity. The servos are attached to the jet water tank and covered with a sealed 3D printed faring, connected to the wings through sealed bearings. Control electronics are contained in a separate fuselage section attached to the gas tank which allows the gas tank to be removed easily for charging. Finally, the vehicle is fitted with four unactuated tail fins, located at the end of the water tank. The total mass of the robot is 100.8 grams.

V. Static Performance

Static thrust was measured by mounting the robot vertically to a load cell, with force data recorded at 2500Hz (Fig. 7). The sensor was zeroed with the jet water tank full, so weight reduction as water is expelled was also measured by the force sensor. The model output has been modified to show this effect in the predicted force profile shown in Fig. 7. Thrust profiles were recorded for six actuations, with the final actuation conducted with the jet immersed in water. The measured thrust profiles show the expected features of a rapid rise in pressure before the water accelerates, followed

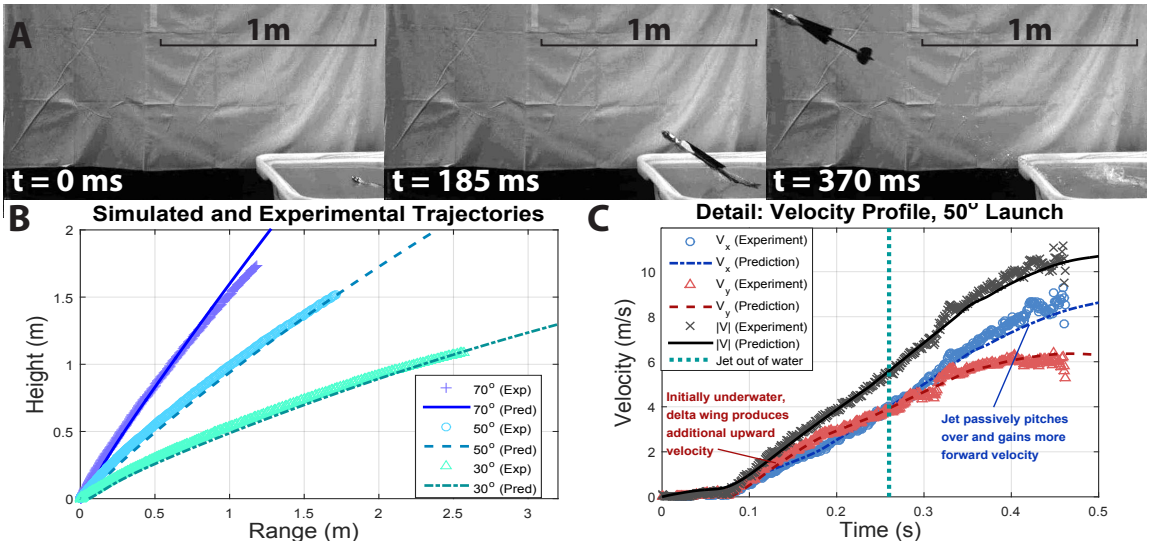


Fig. 8: Aquatic Take-off Tests. A: Stills from 800fps launch video (30^o launch angle), 185ms apart. B: Tracked trajectories, at 30^o, 50^o and 70^o. C: Velocity during a 50^o launch, showing vertical and horizontal components.

by water discharge at sustained pressure and a tapering off of thrust as remaining gas is expelled.

The thrust shows good consistency between repetitions. The discrepancies observed are likely due to a change in the temperature of the CO_2 tank used for charging. The vapour pressure of CO_2 is 57bar at 20^{o}C, but this varies by approximately 1.25bar/^{o}C, and the cooling of the capsule due to liquid CO_2 evaporation during charging or changes in ambient conditions will vary initial pressure between tests.

Towards the end of the water expulsion, the velocity of the air-water interface increases rapidly as it passes through the nozzle contraction. At this point, fluid wall shear and 'plughole' vortical instabilities allow air to mix with water and escape before all water has been expelled, resulting in a spray rather than a jet. The effect of this spraying can be observed as increased measured thrust due to extra mass flow, compared to the gas only theoretical prediction (Fig. 7). No significant variation in thrust when actuating underwater was expected, which was confirmed by the sixth static thrust test, conducted underwater. The only appreciable difference was the increased noise in the thrust profile after air begins to mix with the water outflow.

VI. Aquatic Takeoff Performance

After thrust was recorded, the AquaMAV was launched from a water tank into flight. The jet has slight positive buoyancy, and so was allowed to float freely on the surface. To validate the trajectory model, the launch angle was varied by resting the robot tail on submerged platforms of varying height. Trajectories were tracked using 800fps video. The jet was directed to impact a net 4.5m away from the launch point, which did not allow for a significant gliding phase to be recorded. To allow longer trajectories, the AquaMAV was also launched from a nearby lake and filmed, although tracking was not possible.

Indoor tests showed that the trajectory model was able to accurately predict the AquaMAV's take-off (Fig. 8), and demonstrated that the jet could readily achieve speeds of over 11m/s, more than enough for transition to flight. The model predicts that the delta wing will generate hydrodynamic lift when in the water, which was captured by the model (Fig. 8C), as was the overall trajectory of the robot in several tests.

During outdoor tests (Fig. 1), the wings were deployed after a preset delay (t_d, Fig. 9A), determined using the trajectory model based on maximising glide distance. Using this simple open loop method only limited gliding

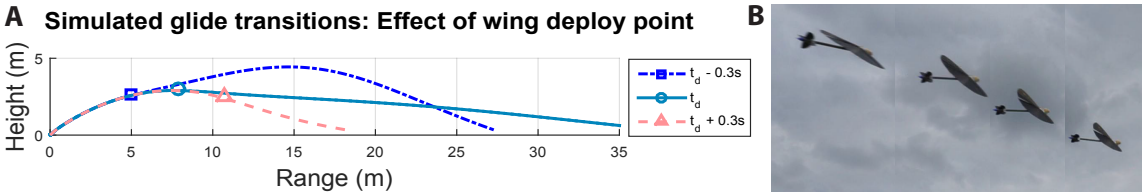


Fig. 9: A: Trajectory simulations for a 50^o launch with glide transition, with the wing deploy point indicated. Without elevator control, changing t_{deploy} significantly effects the trajectory. B: Uncommanded shifting of the left wing after deployment, leading to a crash.

was achieved, and slight variations in trajectory resulted in the robot not having time to passively correct its pitch before hitting the ground (Fig. 1B). The use of separately actuated wings often led to asymmetry between the two wings, rolling the robot (Fig. 9B). In addition, the direct link between servo and wing makes the wings prone to movement in flight; adding bistablity to the mechanism would improve rigidity and performance.

VII. Discussion

The robot has demonstrated the viability of the design and the reliability of the underlying theory. Significant flight speed from water was achieved in spite of hydrodynamic resistance, and a simple drag model has been shown to provide good predictions of launch trajectories. This model indicates that the robot is able to take-off in the presence of perturbations from surface waves to both its launch angle and depth.

Further work is needed on the transition to gliding flight. Principally, effective take off will require some control, as even though flight speed is attainable despite launch perturbations, transitioning to stable, level flight will require attitude estimation. Autononomy is also a necessary part of launching from the water, because the radio frequencies commonly used to communicate with aerial robots have poor penetration into water [23], and reliable communication is difficult subsurface.

The robot weighs slightly more than 100 grams. This includes batteries, electronics, a waterproof fuselage and large lifting surfaces. The addition of servo driven control surfaces to the tail and a propeller for aerial propulsion would not significantly increase take-off weight, and would allow sustained flight from water. The water jet thruster (40% of robot mass) is twice as heavy as is required by design standards due to test safety concerns, and its weight can be reduced without affecting performance. The power consumption of the valve actuation and wing deployment is small (2mAh/launch) and will have little effect on the provision of battery power for flight. The typical range of other MAVs at the 100g scale is around 1 mile, which is also the required range for a water sampling vehicle given in [2].

The SMA valve actuation system has performed over 100 actuations since fabrication, without any noticed loss in performance. The robot is also a lightweight, self-actuated compressed gas storage system, with a 90 bar release capacity (limited by SMA yield), a system which has many potential applications outside of propulsion, such as inflatable structures or buoyancy control.

VIII. Conclusions and Future Work

In this paper we have presented a novel water jet propelled aquatic jumpglider. This AquaMAV has demonstrated powerful aquatic jumps, and to the best of the author's knowledge is the first demonstration of jumpgliding from beneath the water surface. A theoretical model has been developed which will allow mission-specific design of future robots.

Future work will focus on the addition of aerial propulsion, control surfaces and sensing, so that the vehicle can make sustained flights. This will allow the implementation of a plunge diving water sampling and sensing vehicle or a 'self-recovering' long term sensor node, either of which would greatly improve the accessibility of water data.

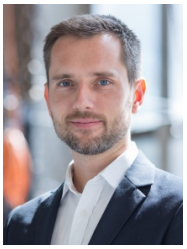
References

[1] R. Siddall and M. Kovač, "Launching the aquamav: bioinspired design for aerial-aquatic robotic platforms," *Bioinspiration & biomimetics*, vol. 9, no. 3, p. 031001, 2014.

[2] J.-P. Ore, S. Elbaum, A. Burgin, and C. Detweiler, "Autonomous aerial water sampling," *Journal of Field Robotics*, vol. 32, no. 8, pp. 1095–1113, 2015.
[3] R. Lock, S. Burgess, and R. Vaidyanathan, "Multi-modal locomotion: from animal to application," *Bioinspiration & Biomimetics*, vol. 9, no. 1, p. 011001, 2014.
[4] A. Crespi, K. Karakasiliotis, A. Guignard, and A. J. Ijspeert, "Salamandra robotica ii: an amphibious robot to study salamander-like swimming and walking gaits," *Robotics, IEEE Transactions on*, vol. 29, no. 2, pp. 308–320, 2013.
[5] R. Eubank, E. Atkins, and G. Meadows, "Unattended operation of an autonomous seaplane for persistent surface and airborne ocean monitoring," in *OCEANS 2010*. IEEE, 2010, pp. 1–8.
[6] J. Izraelevitz and M. Triantafyllou, "A novel degree of freedom in flapping wings shows promise for a dual aerial/aquatic vehicle propulsor," *arXiv preprint arXiv:1412.3843*, 2014.
[7] A. Vidyasagar, J.-C. Zufferey, D. Floreano, and M. Kovac, "Performance analysis of jump-gliding locomotion for miniature robotics," *Bioinspiration & Biomimetics,* in press, 2015.
[8] A. L. Desbiens, M. T. Pope, D. L. Christensen, E. W. Hawkes, and M. R. Cutkosky, "Design principles for efficient, repeated jumpgliding," *Bioinspiration & biomimetics*, vol. 9, no. 2, p. 025009, 2014.
[9] R. Bachmann, R. Vaidyanathan, F. Boria, J. Pluta, J. Kiihne, B. e. a. Taylor, R. Bledsoe, P. Ifju, and R. Quinn, "A miniature vehicle with extended aerial and terrestrial mobility," in *Flying insects and robots*. Springer, 2010, pp. 247–270.
[10] M. M. Maia, P. Soni, and F. J. Diez, "Demonstration of an aerial and submersible vehicle capable of flight and underwater navigation with seamless air-water transition," *arXiv preprint arXiv:1507.01932*, 2015.
[11] J. Rayner, "Pleuston: animals which move in water and air," *Endeavour*, vol. 10, no. 2, 1986.
[12] K. Muramatsu, J. Yamamoto, T. Abe, K. Sekiguchi, N. Hoshi, and Y. Sakurai, "Oceanic squid do fly," *Marine biology*, vol. 160, no. 5, pp. 1171–1175, 2013.
[13] C. J. Gommes, "A more thorough analysis of water rockets: Moist adiabats, transient flows, and inertial forces in a soda bottle," *American Journal of Physics*, vol. 78, p. 236, 2010.
[14] *BS EN 60534-2-1, Process Control Valves*, 2011.
[15] P. Thomas, *Simulation of Industrial Processes for Control Engineers*. Elsevier Science, 1999.
[16] *Cores and Caps for Industrial Applications*. Schrader S.A.S., 2011.
[17] E. C. Polhamus, *A concept of the vortex lift of sharp-edge delta wings based on a leading-edge-suction analogy*. National Aeronautics and Space Administration, 1966.
[18] S. Hoerner, *Fluid-dynamic drag*, 1965.
[19] M. Shiffman and D. Spencer, "The force of impact on a cone striking a water surface (vertical entry)," *Communications on pure and applied mathematics*, vol. 4, no. 4, pp. 379–417, 1951.
[20] *BS EN 13445-3, Unfired Pressure Vessels*, 2015.
[21] *Flexinol Technical Data*. Dynalloy Inc., 2007.
[22] C. Wang, *Applied elasticity*. McGraw-Hill, 1953.
[23] J. Yuh and M. West, "Underwater robotics," *Advanced Robotics*, vol. 15, no. 5, pp. 609–639, 2001.



Robert Siddall is a PhD candidate in the Department of Aeronautics at Imperial College London, working in the Aerial Robotics Laboratory. He received his MEng degree from the University of Cambridge, Cambridge, UK in 2012. His work focusses on multimodal mobility, in particular the design of miniature robots able to move in both air and water.



Mirko Kovac is the director of the Aerial Robotics Laboratory and lecturer in Aero-structures at Imperial College London. He was a post-doctoral researcher in the Wyss Institute at Harvard University, Cambridge, USA. He obtained his PhD from the Swiss Federal Institute of Technology (EPFL), in Lausanne, Switzerland in 2010 and his M.S. and B.S. degree from the Swiss Federal Institute of Technology (ETH) in Zurich.